Coupling of Fluids, Solids and Waves Problems in Aeronautics, Springer 2002

Computational Bluff Body Fluid Dynamics and Aeroelasticity

H. M. Blackburn
CSIRO Building Construction and Engineering,
PO Box 56, Highett 3190, Australia
hugh.blackburn@csiro.au

Summary

Computational approaches are now making a substantial contribution to investigations in bluff body fluid mechanics, which were previously the sole domain of experimentalists. Stability analysis, direct numerical simulation and, increasingly, large eddy simulation, is being used to study fundamental aspects of the phenomena involved. Accelerating reference frame solution techniques have recently been developed and employed in the study of bluff body aeroelasticity: these are described and applied to the study of flows past slender cylinders with prescribed motion, and with aeroelastic fluid–structure interaction.

1 Introduction

Bluff body fluid dynamics and aeroelasticity differ from more classical studies in aeroelasticity primarily because the extensive regions of separated flow inherent in the problems under study defy compact theoretical treatment. For this reason, progress is heavily dependent on experimental approaches, both physical and numerical. As noted by the editors of a recent collection of works in the area [1], computational fluid dynamics is now making a significant contribution to fundamental understanding in bluff body fluid dynamics, owing to the ability to control and observe independent and dependent variables in ways that are difficult or impossible to achieve in physical experiments.

In this paper we describe 'accelerating reference frame', or ARF, techniques — a class of methods that recently has been successfully applied to studies of bluff body fluid–structure interaction problems. Example results from computational studies of interaction between vortex street wakes and circular cylinders are reviewed. Finally, we outline prospects for future work in the area.

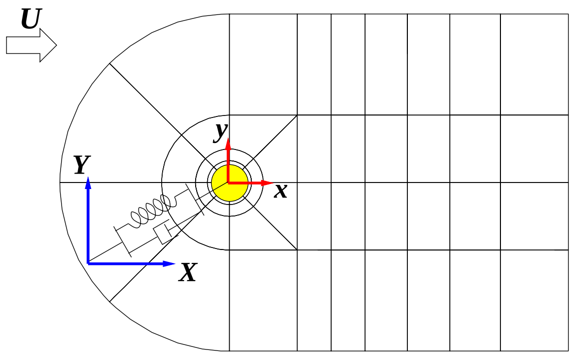

Figure 1 Schematic illustrating the basis of accelerating reference frame (ARF) techniques. Flows are solved in an ARF attached to the structure: the mesh moves with the structure, does not distort with time, and is coupled through motion-dependent forces to a global reference frame in which the far-field flow $\boldsymbol{U}$ is prescribed.

2 Computational Methods

An elastic structure will distort in response to loads exerted on it by a flowing fluid, and when the motion of the structure can feed back to affect the flow, an aeroelastic coupling arises. In analysis techniques, separate discretisations of the fluid and the structure are typically employed, and the problems are coupled through boundary conditions. Here we will focus on the fluid-mechanical part of the problem and assume that the dynamic structural motion can be obtained through any appropriate technique.

Two basic methods of approach can be identified for mesh-based numerical discretisations of the flow problems. The most general approach allows the computational mesh local to the structure to distort continuously in time as the structure moves. In this case, the far-field boundaries of the mesh, and the associated boundary conditions, are usually kept fixed in time. This is the 'arbitrary Lagrangian–Eulerian', or ALE approach. However, the method has significant computational overheads associated with the temporal changes of the mesh interpolation functions. An alternative is leave the mesh unchanged in time, but fix it to the structure and allow it to move in space, adjusting the momentum equations and boundary conditions as appropriate. This is the 'accelerating reference frame' or ARF, approach, as illustrated schematically in Figure 1. For open flows past an isolated structure, ARF methods can be just as appropriate as ALE methods, and avoid computational overheads associated with mesh distortion.

2.1 ARF Techniques for Fluid–Structure Interaction

Consider the interaction between an essentially two-dimensional slender elastic structure and the (possibly three-dimensional) flow past it. The structure is characterised by its mass per unit length m, natural frequency $f_\mathrm{n} = \omega_\mathrm{n}/2\pi$ and dimensionless structural damping ζ, and it carries a set of reference frame axes. In an inertial, global, reference frame, the structure moves in response to the force per unit length $\boldsymbol{f}$ exerted on it by the fluid, according to

$$\ddot{\boldsymbol{x}} + 2\zeta\omega_\mathrm{n}\dot{\boldsymbol{x}} + \omega_\mathrm{n}^2\boldsymbol{x} = \boldsymbol{f}/m \tag{1}$$

or as a set of first-order ODEs, with $\boldsymbol{v} = \dot{\boldsymbol{x}}$

$$\dot{\boldsymbol{v}} = \boldsymbol{f}/m - 2\zeta\omega_n\boldsymbol{v} - \omega_\mathrm{n}^2\boldsymbol{x}, \qquad \dot{\boldsymbol{x}} = \boldsymbol{v}. \tag{2}$$

The equations that describe the *relative* motion of incompressible fluid of density ρ in the reference frame attached to the structure are

$$\partial_t\boldsymbol{u} + \boldsymbol{N}(\boldsymbol{u}) = -\rho^{-1}\nabla p + \nu\nabla^2\boldsymbol{u} - \nabla\cdot\boldsymbol{\tau} - \ddot{\boldsymbol{x}}, \qquad \nabla\cdot\boldsymbol{u} = 0, \tag{3}$$

where $\boldsymbol{u}$ is the velocity field, $\boldsymbol{N}(\boldsymbol{u})$ represents nonlinear advection terms, and $\boldsymbol{\tau}$ is a possible sub-grid scale stress in the case of a large eddy simulation. Note the direct coupling of (3) to (1) through the frame acceleration $\ddot{\boldsymbol{x}}$.

At domain boundaries where far-field velocity boundary conditions, $\boldsymbol{U}$, are prescribed in the inertial reference frame, the appropriate conditions in the ARF are

$$\boldsymbol{u} = \boldsymbol{U} - \boldsymbol{v}. \tag{4}$$

On the surface of the structure, the velocity boundary condition is typically $\boldsymbol{u} = 0$. Pressure boundary conditions, if required, are obtained by dotting the domain unit outward normal $\boldsymbol{n}$ into (3); employing also the vector identity $\nabla^2\boldsymbol{u} = \nabla(\nabla\cdot\boldsymbol{u}) - \nabla\times\nabla\times\boldsymbol{u}$ provides

$$\partial_n p = \rho\,\boldsymbol{n}\cdot\left[-\boldsymbol{N}(\boldsymbol{u}) - \nu\nabla\times\nabla\times\boldsymbol{u} - \nabla\cdot\boldsymbol{\tau} - \ddot{\boldsymbol{x}} - \partial_t\boldsymbol{u}\right]. \tag{5}$$

Two special cases of (5) occur: on the far-field boundary, $\partial_t\boldsymbol{u} = -\ddot{\boldsymbol{x}}$, while, on the surface of the structure, often $\partial_t\boldsymbol{u} = \boldsymbol{u} = 0$.

Coupling of (1) back to (3) occurs through the force per unit length exerted by the fluid on the structure through pressure and viscous stress

$$\boldsymbol{f} = \oint p\boldsymbol{n}\,\mathrm{d}s - \oint \mu\boldsymbol{n}\cdot\left[\nabla\boldsymbol{u} + (\nabla\boldsymbol{u})^T\right]\,\mathrm{d}s, \tag{6}$$

where the integrals are taken around the surface perimeter of the structure.

These techniques can also be applied to cases where the structure has prescribed motion, in which case $\dot{\boldsymbol{x}}$ and $\ddot{\boldsymbol{x}}$ are explicitly supplied.

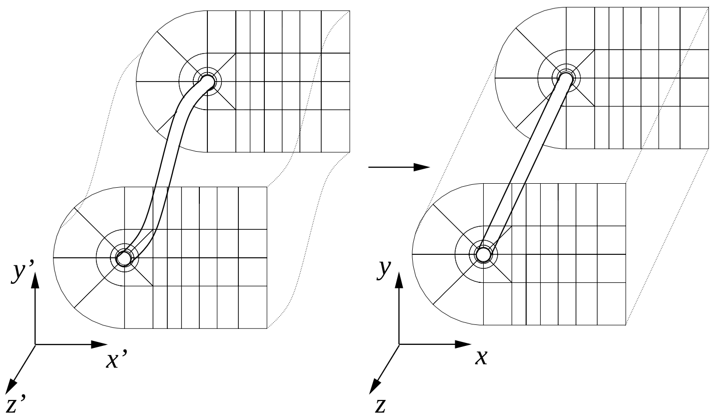

Figure 2 Schematic used to illustrate the application of ARF techniques to cases in which the structure deforms in directions normal to its axis. Coupling terms are computed on the basis of the mapping $\boldsymbol{x} \rightarrow \boldsymbol{x}'$.

2.2 Generalised ARF Techniques

ARF techniques as described above were first applied to the study of vortex-induced vibration of circular cylinders [2, 3, 4]. An extension allows the same technique to be applied in cases where the flexible structure has a rotational degree of freedom in addition to translational freedoms [5].

The method has also been generalised to the case where the displacement of the structure varies in the third dimension, as illustrated in Figure 2 [6]. If the mapping that takes the position of a point on the structure, $\boldsymbol{x}'$, into a system of coordinates in which the structure is undistorted, $\boldsymbol{x}$, is given by

$$x = x' - \zeta(z,t), \quad y = y' - \eta(z,t), \quad z = z', \tag{7}$$

then the corresponding velocity components and the pressure are related by

$$u = u' - \partial_t \zeta - w\partial_z \zeta, \quad v = v' - \partial_t \eta - w\partial_z \eta, \quad w = w', \quad p = p'. \tag{8}$$

This transformation supplies additional pressure and viscous coupling terms to (3), which becomes

$$\partial_t \boldsymbol{u} + \boldsymbol{N}(\boldsymbol{u}) = -\rho^{-1}\nabla p + \nu\nabla^2 \boldsymbol{u} + \boldsymbol{A}(\boldsymbol{u}, p, t), \tag{9}$$

with

$$A_x = -\mathrm{d}_{tt}\zeta + \nu\left[\partial_{z'z'}\left(u + w\partial_z\zeta\right) - \partial_{zz}u + \partial_z\zeta\nabla^2_{xy}w + \partial_{tzz}\zeta\right], \tag{10a}$$
$$A_y = -\mathrm{d}_{tt}\eta + \nu\left[\partial_{z'z'}\left(v + w\partial_z\eta\right) - \partial_{zz}v + \partial_z\eta\nabla^2_{xy}w + \partial_{tzz}\eta\right], \tag{10b}$$
$$A_z = \partial_z\zeta\partial_x p + \partial_z\eta\partial_y p + \nu\left[\partial_{z'z'}w - \partial_{zz}w\right], \tag{10c}$$

where the operators

$$
\begin{aligned}
\mathrm{d}_t &\equiv \partial_t + u\partial_x + v\partial_y + w\partial_z, && \text{(11a)}\\
\partial_{z'} &\equiv \partial_z - \partial_z\zeta\partial_x - \partial_z\eta\partial_y, && \text{(11b)}\\
\nabla^2_{xy} &\equiv \partial_{xx} + \partial_{yy}. && \text{(11c)}
\end{aligned}
$$

Now that the structure has a third degree of freedom, partial differential equations, derived e.g. from beam theory, replace the ODEs (1).

2.3 Discretisations

ARF techniques can be allied with any suitable spatial discretisation or temporal integration methods. In the applications to be described here, spectral elements have been used for spatial discretisations, in conjunction with mixed explicit–implicit time integration [7], usually of second order.

3 Prescribed Motion

First we review some studies of flows either past or generated by circular cylinders with prescribed oscillation. In each case the focus of the study has been to examine flow phenomena through numerical investigations that would be difficult or impossible to replicate through physical experiments.

3.1 Phase Switching in the Wake of an Oscillating Cylinder

The purpose of this study [8] was to investigate the mechanism underlying 'phase switching' that occurs in the wake of a circular cylinder forced to oscillate cross flow. In the primary synchronisation regime, when the Kármán wake oscillation frequency is entrained by that of cross flow oscillation, it is known from experimental studies that a rapid variation in the phase angle between cylinder motion and lift force occurs over a narrow range of cylinder motion frequencies. This phase switch is accompanied by a change in sign of the time-average mechanical energy transfer between the structure and fluid.

The mechanical energy transferred from the flowing fluid, freestream speed U, to the oscillating cylinder, diameter D, per motion cycle, period T, can be written in dimensionless form as

$$
E = \frac{2}{\rho U^2 D^2}\int_0^T \dot{y}F_l\,\mathrm{d}t = \int_0^T \dot{\alpha}C_l\,\mathrm{d}t = \frac{1}{2}\oint\left(C_l\,\mathrm{d}\alpha + \alpha\,\mathrm{d}C_l\right), \qquad (12)
$$

where $\alpha = y/D$ is the dimensionless cross flow displacement, F_l is the cross-flow force per unit length and C_l the corresponding lift coefficient. The quantity E is positive when work is done on the cylinder, negative when work is done on the fluid. The last term in (12) assumes that a time-periodic solution has been obtained; the path integrals are taken around a limit cycle

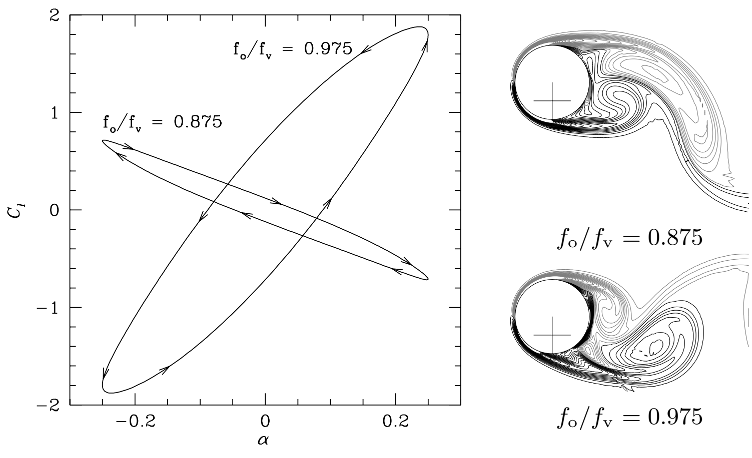

Figure 3 Limit cycles of coefficient of lift vs. dimensionless cross flow displacement for two-dimensional flow past an oscillating cylinder, $Re = 500$, $\alpha_{\max} = 0.25$ [8]. The dimensionless energy transfer between the cylinder and the fluid per motion cycle (E) is given by the area enclosed by the cycle, and its sign by the orientation of traverse. E is positive for $f_o/f_v = 0.875$, negative for $f_o/f_v = 0.975$. Also shown are the corresponding vorticity contours, displayed at the point of maximum cylinder displacement.

in (α, C_l) space. Figure 3 shows two of these limit cycles, obtained from two-dimensional simulations at $Re = 500$ and an amplitude ratio $\alpha_{\max} = 0.25$, and at two different frequency ratios $f_o/f_v = 0.875$ and 0.975, where f_o is the imposed cross flow oscillation frequency and f_v is the fixed-cylinder vortex shedding frequency. The orientation of traverse around the limit cycles, and hence the sign of E, is opposite in the two cases. Also shown in Figure 3 are contours of vorticity for these two frequency ratios, computed at the same phase in the cylinder motion cycle, illustrating the fact that the timing of vortex shedding is also changed dramatically by variation in f_o/f_v.

An hypothesis was advanced that the change in flow structure between the two types of solution illustrated in Figure 3 resulted from a change in balance between two different vorticity production mechanisms, one associated with surface-tangential pressure gradients, the other with the tangential component of cylinder acceleration. This hypothesis was investigated by numerically manipulating the local tangential motion of the cylinder boundary to reduce the motion-induced vorticity production progressively to zero. As this was done, the solution branch associated with the flow shown for $f_o/f_v = 0.975$ became smaller in extent, and eventually disappeared altogether when the motion-induced vorticity production was zero, while the extent of the other solution branch was left comparatively unchanged. The outcome of this numerical experiment thus appears to support the hypothesis.

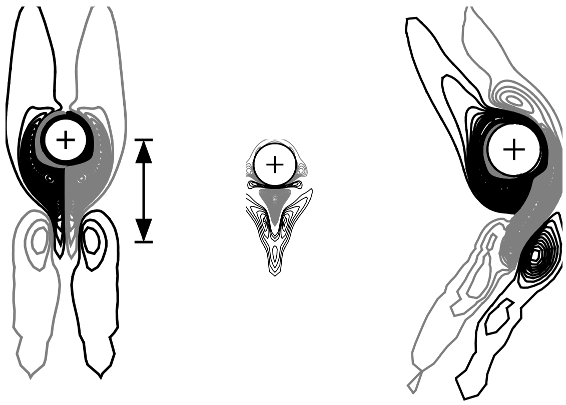

Figure 4 Vorticity contours for the two-dimensional flows produced by a cylinder in vertical oscillation of indicated amplitude, $KC = 7$. For $\beta = 13.5$, the two-dimensional periodic flow shown in (a) is linearly unstable to the two-dimensional symmetry breaking Floquet mode shown in (b), leading to another periodic two-dimensional flow, but with broken reflection symmetry, illustrated in (c). The two-dimensional asymmetric periodic flows are further unstable to three-dimensional Floquet modes [9]. The symmetric base flow, its unstable Floquet mode, and the resulting asymptotic flow are all presented at the phase of maximum oscillation amplitude, $\alpha_{\max}$.

3.2 Instability of the Flow Generated by an Oscillating Cylinder

The oscillatory rectilinear translation of a long circular cylinder normal to its axis in a quiescent body of fluid at low motion amplitudes and frequencies generates a time-mean streaming flow which is inwards towards the low-pressure shoulders of the moving cylinder and outwards along the motion axis. The two dimensionless groups that describe the problem are the Keulegan–Carpenter number $KC = 2\pi\alpha_{\max}$ and Stokes number $\beta = f_{\mathrm{o}}D^2/\nu$. At low values of KC and β, the flow is time-periodic, two-dimensional and has reflection symmetry about the translation axis, as shown in Figure 4 (a). Increasing either KC or β can lead to three-dimensional flows through either of two instability mechanisms [9]. As the two-dimensional flow is time-periodic, Floquet analysis is the appropriate tool with which to study the problem.

At low values of β, increasing KC leads to instability of a two-dimensional Floquet mode that breaks the reflection symmetry about the translation axis (Figure 4 b); the subsequent asymmetric periodic flows (Figure 4 c) are further unstable to three-dimensional Floquet modes. At low values of KC, increasing β produces instability of three-dimensional Floquet modes that break the cylinder-axis translation symmetry, leading to a three-dimensional flow that retains reflection symmetry in the spanwise average.

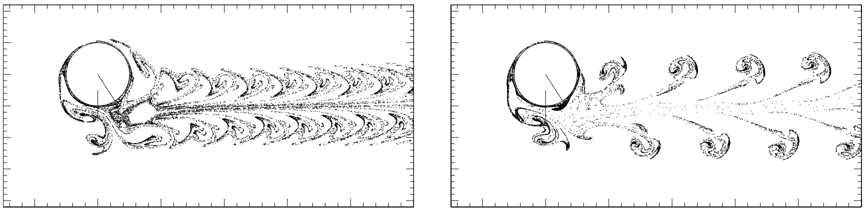

(a) (b)

Figure 5 Particle-tracking visualisations of the two-dimensional flows produced by a circular cylinder which has a vertical translational oscillation combined with a rotational oscillation [10]. Flows generated (a), when the cylinder does not translate in the horizontal direction; (b), with the cylinder swimming to left at its terminal speed. $Re_{\mathrm{rms}} = 200$, based on vertical oscillation velocity.

3.3 Propulsion Produced by Oscillatory Rotation and Translation

In [10], it was reported that when a oscillatory rotation of the cylinder is added to the rectilinear oscillatory translation (as in § 3.2), a new streaming flow can result. If the periods of the two motions are the same, and the phase angle between them set appropriately, the time-mean streaming flow is directed outwards along a line *perpendicular* to the cylinder translation axis, as seen in Figure 5 (a). Thus results a time-mean force in a direction normal to the cylinder translation axis. If the cylinder is left free to accelerate in the direction normal to the imposed oscillatory motion, it can gain speed and eventually will swim at a terminal mean velocity, producing the flow illustrated in Figure 5 (b). For two-dimensional flows, the asymptotic state is time-periodic and again amenable to Floquet analysis, which shows three-dimensionally-unstable Floquet modes.

4 Coupled Fluid–Structure Problems

4.1 Mass-Damping Effects

An early application of the ARF method in aeroelastic studies was to two-dimensional flow past a flexibly mounted circular cylinder at $Re = 200$ [2]. The structural oscillation frequency f_{n} was set to match the vortex shedding frequency for the fixed cylinder. The remaining dimensionless groups are then the structural damping ratio ζ and the density ratio $m/\rho D^2$. These may be combined into a single mass-damping parameter of the form $m\zeta/\rho D^2$, often used to correlate the observed maximum amplitude of cross flow response, as in Griffin's compilation of experimental results [11], shown in Figure 6. As the damping $\zeta \rightarrow 0$, the peak amplitudes asymptote to maximum values, and the simulation results, also plotted in Figure 6, show that these are only weakly dependent on the density ratio.

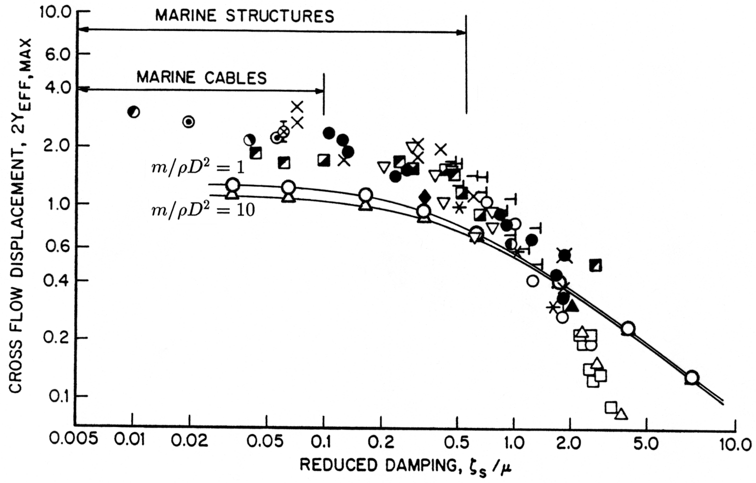

Figure 6 Maximum values of asymptotic peak-to-peak free vibration oscillation amplitudes as functions of the mass-damping product $\zeta_s/\mu = 8\pi^2 St^2 m\zeta/\rho D^2$ [2]. A comparison of computed values for density ratios $m/\rho D^2 = 1$ (○) and 10 (△), $Re = 200$, with a compilation of experimental values [11]

4.2 Lock-In Effects

In order to study the effect of variation of the ratio of structural natural frequency to fixed-cylinder vortex shedding frequency, another set of two-dimensional simulations was carried out [3], in this case with the damping and density ratios set to $\zeta = 0.01$ and $m/\rho D^2 = 10$ respectively. For these simulations, the Reynolds number was fixed at $Re = 250$. The results are summarised in Figure 7.

For all simulations, cylinder cross-flow oscillation and lift frequencies were found to coincide in the asymptotic state, however the lift/oscillation frequency f_o was nearly the same as f_v away from $f_\mathrm{n}/f_\mathrm{v} = 1$. Near $f_\mathrm{n}/f_\mathrm{v} = 1$ both frequencies changed together to fall near (but not *exactly* on) f_n: exact coincidence with f_n is indicated by the slanted thin line near the centre of the figure. This change in vortex shedding frequency to nearly match the cylinder natural frequency is the lock-in phenomenon. During lock-in, amplitudes of cross-flow oscillation increased markedly: the largest steady-state values correspond to peak-to-peak oscillation amplitudes of approximately $0.9\,D$ (rms values of α are presented in Fig. 7). The lack of exact coincidence of f_o with f_n during lock-in can be accounted for by a phase difference between cylinder motion and lift forces, which is known to be a function of $f_\mathrm{n}/f_\mathrm{v}$.

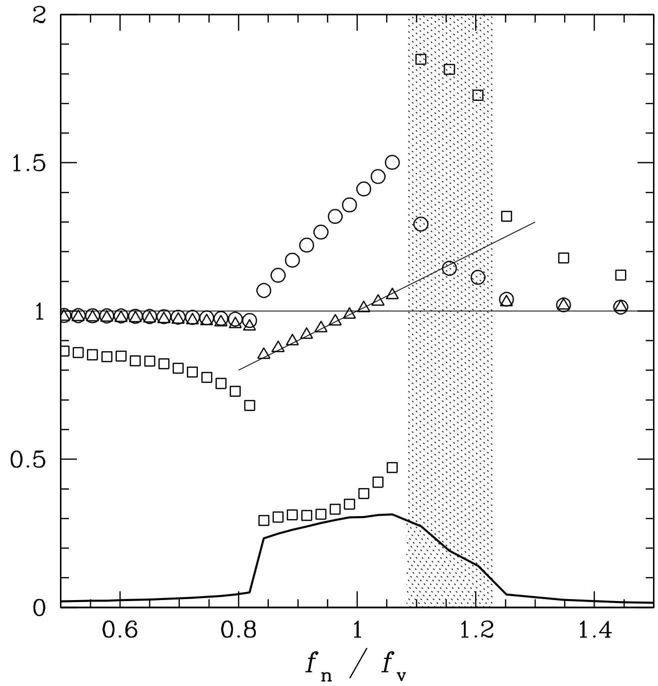

Figure 7 Cylinder response diagram for two-dimensional simulations at $Re = 250$ [3]. Abscissa values give the ratio of cylinder *in vacuo* natural frequency f_{n} to Strouhal frequency for the fixed cylinder f_{v}. $\square$, ratio of fluctuating lift coefficients $C_{\mathrm{l_{rms}}}/C_{\mathrm{l_{rms_0}}}$; $\circ$, ratio of mean drag coefficients $C_{\mathrm{d}}/C_{\mathrm{d_0}}$; $\triangle$, ratio of oscillation frequency to fixed-cylinder Strouhal frequency $f_{\mathrm{o}}/f_{\mathrm{v}}$; ——, cylinder cross-flow response amplitude α_{rms}. Shaded region indicates a chaotic response regime.

4.3 Three-Dimensional Wake Effects

The simulations in §§ 4.1 and 4.2 were for two-dimensional flows, whereas since fixed-cylinder wakes become three-dimensional for Reynolds numbers above approximately 190, effectively all real-world occurrences of vortex-induced vibrations of circular cylinders must involve three-dimensional wake flows. Two-dimensional simulations, while significant, can potentially fail to reveal effects of dynamically important flow physics. With increases in computer capacity, full three-dimensional DNS and LES studies can now be undertaken, however these are still expensive, owing to the long integration times involved.

Figure 8, reproduced from [4], compares cylinder cross flow amplitude responses obtained using physical experiments with those obtained using both two-dimensional and three-dimensional simulations, where all relevant pa-

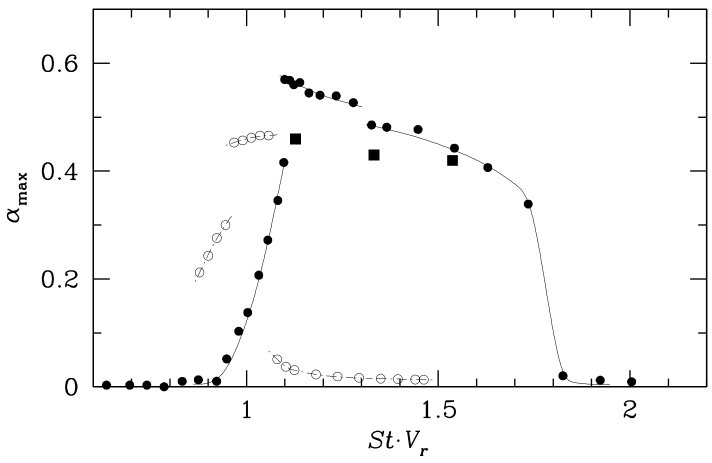

Figure 8 Dimensionless average peak response amplitude $\alpha_{\max}$ in vortex-induced vibration of a circular cylinder as a function of dimensionless flow speed $St \cdot V_{\mathrm{r}}$ for $Re \simeq 750$ [4]: •, experimental results; ■, three-dimensional simulations; ∘, two-dimensional simulations.

rameter values (Re, $m/\rho D^2$, ζ) were matched. The flow speed is given dimensionlessly as $St \cdot V_{\mathrm{r}}$, where $St = f_{\mathrm{v}} D/U$ is the fixed-cylinder Strouhal number and $V_{\mathrm{r}} = U/f_{\mathrm{n}} D$ is the reduced velocity. It is clear that the nature of the responses for two-dimensional simulations and experiment are very different, in terms of peak amplitudes achieved, but particularly in the number and extent of observed solution branches. The three comparable values obtained using three-dimensional DNS reveal much better agreement with experiment in terms of the extent and position of the response amplitude envelope.

The comparison of response amplitudes obtained with three-dimensional DNS with those obtained experimentally is encouraging, although there are significant differences and a more extensive study is desirable. However, another important point of comparison is of the coherent structures of the wake flows. No two-dimensional DNS result has been able to reproduce the experimentally observed '2P' wake mode, where two counter-rotating pairs of vortices are formed in the near wake for each cylinder motion cycle. Figure 9 shows a comparison of phase-averaged contours of the spanwise vorticity component in the near wake, obtained from DNS and from physical experiments (though at a slightly higher Re). It is clear that the simulations reproduce the '2P' wake mode observed in the experiment.

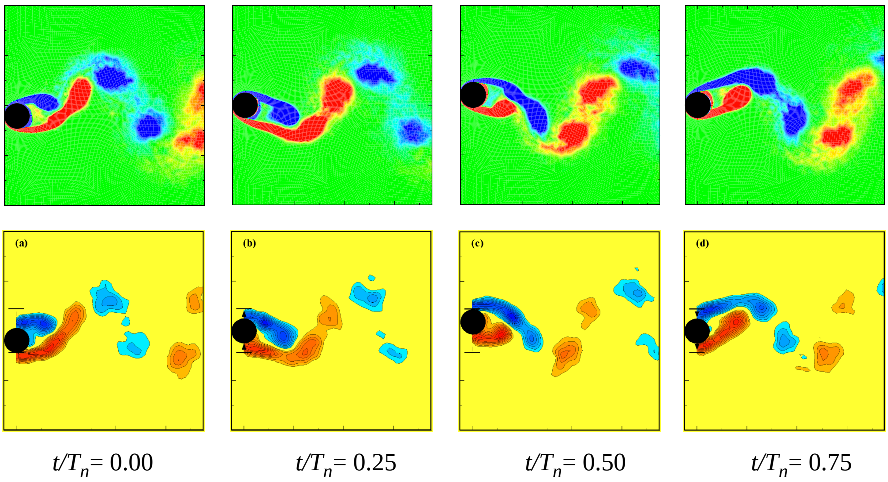

Figure 9 Simulation results showing phase and spanwise average contours of spanwise vorticity for four phases of the cylinder motion cycle at $Re \simeq 750$ (upper plots), compared to (lower) similar (two-dimensional) phase averages from experiments at a slightly higher Reynolds number [4].

Table 1 Global flow parameters from LES of flow past a fixed cylinder at $Re = 3900$ compared to experimental values at $Re = 3000$.

Source	St	C_{pb}	C_d
Norberg [13]	0.210	-0.88	0.99
Spectral element LES	0.218	-0.93	1.01

5 Stationary Bluff Body Flows

We complete our survey of computational bluff-body fluid dynamics by noting that while most of the recent fundamental computational investigations in the area have used direct numerical simulation techniques, progress to more applicable Reynolds numbers requires some form of turbulence modelling. In view of the relative infancy of turbulence models applied to bluff-body flows, large eddy simulations would appear to be the most promising avenue for extension in this area. Results from eddy-viscosity based LES of flow past a stationary circular cylinder, $Re = 3900$ [12], are presented in Table 1 and Figure 10. The relatively good agreement with the available validation data encourages further development — but more detailed comparisons also serve to highlight the need for more extensive validation experiments.

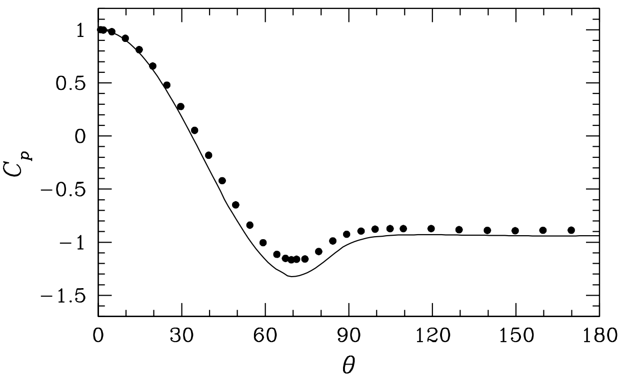

Figure 10 Time-mean pressure coefficient on the surface of a stationary cylinder as a function of angular position, LES results for $Re = 3900$ [12]. ——, spectral element simulation; •, experimental results for $Re = 3000$ [13].

6 Discussion and Prospects

The immediate prospects for application of ARF methods are to moderate Reynolds number flows through adoption of LES approximations in the flow solver. This will allow more direct comparison with experimental results, and after this validation to better understanding of bluff-body vortex-induced vibration. The path is also open to better understanding of buffeting and quasi-steady aeroelastic effects such as stall-flutter and galloping.

While the applications of ARF techniques here have all been to separated flows, they can equally be applied to DNS or LES of aeroelastic fluid–structure interaction of attached flows. We can also anticipate extensions of the method to deal with fully three-dimensional structures. Finally, the ARF approach can be applied to any problem where the flow can be described in an accelerating reference frame. An intriguing example presently under study is the violent overturning instability in a spinning, precessing container of fluid [14].

Acknowledgments

Research in this area has been made more pleasurable through interaction with my colleagues. I gratefully acknowledge the contribution of my collaborators in the work described here: John Elston, Raghuraman Govardhan, Ron Henderson, George Karniadakis, Richard Manasseh, Stefan Schmidt, John Sheridan and Charles Williamson. The support of APAC and CSIRO HPCCC computing facilities has been essential for this work, and I thank their staff for continued support.

References

[1] T. Leweke, P. W. Bearman, and C. H. K. Williamson, "Preface — Special Issue on Bluff Body Wakes and Vortex-Induced Vibrations," J. Fluids & Structures **15,** 377–8 (2001).

[2] H. M. Blackburn and G. E. Karniadakis, "Two- and Three-Dimensional Simulations of Vortex-Induced Vibration of a Circular Cylinder," In *3rd Intnl Offshore & Polar Engng Conf.*, **III,** 715–720 (Singapore, 1993).

[3] H. M. Blackburn and R. D. Henderson, "Lock-In Behaviour in Simulated Vortex-Induced Vibration," Exptl Thermal & Fluid Sci. **12,** 184–189 (1996).

[4] H. M. Blackburn, R. N. Govardhan, and C. H. K. Williamson, "A Complementary Numerical and Physical Investigation of Vortex-Induced Vibration," J. Fluids & Structures **15,** 481–488 (2001).

[5] L. Li, S. J. Sherwin, and P. W. Bearman, "A Moving Frame of Reference Algorithm for Fluid/Structure Interaction of Rotating and Translating Bodies," Intnl J. Num. Meth. Fluids **38,** 187–206 (2002).

[6] D. J. Newman and G. E. Karniadakis, "A Direct Numerical Simulation of Flow Past a Freely Vibrating Cable," J. Fluid Mech. **344,** 95–136 (1997).

[7] G. E. Karniadakis, M. Israeli, and S. A. Orszag, "High-Order Splitting Methods for the Incompressible Navier–Stokes Equations," J. Comput. Phys. **97,** 414–443 (1991).

[8] H. M. Blackburn and R. D. Henderson, "A Study of Two-Dimensional Flow Past an Oscillating Cylinder," J. Fluid Mech. **385,** 255–286 (1999).

[9] J. R. Elston, J. Sheridan, and H. M. Blackburn, "The Transition to Three-Dimensionality in the Flow Produced by an Oscillating Circular Cylinder," In *14th Australasian Fluid Mechanics Conference*, (Adelaide, 2001).

[10] H. M. Blackburn, J. R. Elston, and J. Sheridan, "Bluff Body Propulsion Produced by Combined Rotary and Translational Oscillation," Phys. Fluids **11,** 4–6 (1999).

[11] O. M. Griffin, J. H. Pattison, R. A. Skop, S. E. Ramberg, and D. J. Meggitt, "Vortex-Excited Vibrations of Marine Cables," ASCE J. Wat. Port, Coastal Ocean. Div. **WW2,** 183–204 (1980).

[12] H. M. Blackburn and S. Schmidt, "Large Eddy Simulation of Flow Past a Circular Cylinder," In *14th Australasian Fluid Mechanics Conference*, (Adelaide, 2001).

[13] C. Norberg, "Effects of Reynolds Number and Low-Intensity Freestream Turbulence on the Flow Around a Circular Cylinder," Technical Report No. 87/2, Dept Appl. Thermodyn., Chalmers Univ. Tech. (1987) .

[14] R. Manasseh, "Breakdown Regimes of Inertia Waves in a Precessing Cylinder," J. Fluid Mech. **243,** 261–296 (1992).